

Tuning of nanocavity optomechanical coupling using a near-field fiber probe

AARON C. HRYCIW,¹ MARCELO WU,^{2,3} BEHZAD KHANALILOO,^{2,3} AND PAUL E. BARCLAY^{2,3,*}

¹nanoFAB Facility, University of Alberta, Edmonton, Alberta T6G 2R3, Canada

²National Institute for Nanotechnology, Edmonton, Alberta T6G 2M9, Canada

³Department of Physics and Astronomy and Institute for Quantum Science and Technology, University of Calgary, Calgary, Alberta T2N 1N4, Canada

*Corresponding author: pbarclay@ucalgary.ca

Received 20 February 2015; revised 23 April 2015; accepted 23 April 2015 (Doc. ID 235041); published 14 May 2015

Optomechanical coupling in a nanocavity formed between two cantilevers is tuned through renormalization of the nanocavity field, allowing reconfiguration of the dominant optomechanical transduction mechanism and spatially selective optical readout of mechanical resonances. Tuning is mediated through evanescent interaction between the nanocavity and a fiber taper near-field probe that induces both dissipative and dispersive optomechanical coupling. Tunable optomechanical coupling can exceed 3 GHz/nm, and is shown to allow readout of out-of-plane cantilever nanomechanical resonances suitable for sensing applications. © 2015 Optical Society of America

OCIS codes: (050.5298) Photonic crystals; (350.4238) Nanophotonics and photonic crystals; (130.6010) Sensors; (130.3120) Integrated optics devices.

<http://dx.doi.org/10.1364/OPTICA.2.000491>

Nanocavity optomechanical devices [1–6] confine light within wavelength-scale volumes, where it can interact with nanomechanical resonances whose displacement profiles strongly overlap with the optical field. Among many recent milestone demonstrations, nanophotonic optomechanical devices have been used for sensing [5,7–11], integrated photonics [4,12,13], and fundamental studies of quantum nanomechanical structures [14,15]. The optomechanical coupling strength central to the performance these devices is geometry dependent, and may vanish if the spatial symmetry of the optical and mechanical resonances of interest differs. Here we demonstrate that a near-field probe can be used to reconfigure the optomechanical properties of a nanocavity, enhancing the readout of mechanical resonances with no intrinsic optomechanical coupling. An optical fiber taper waveguide positioned in the nanocavity near field is shown to renormalize the nanocavity optical mode, modifying both its sensitivity to individual mechanical resonances and the balance of dissipative and dispersive nanocavity optomechanical coupling processes [16–21]. We show that these effects can result in optomechanical coupling exceeding several GHz/nm to mechanical resonances with no intrinsic optomechanical coupling—including out-of-plane cantilever modes used in atomic force microscopy and magnetometry applications [22]—enabling a wider variety of optomechanical sensing applications. Furthermore, these effects are shown to allow spatially selective measurement of mechanical resonances, providing information describing their spatial localization.

In cavity optomechanical systems, mechanical excitations perturb the local dielectric environment, modifying the dynamical properties of the optical resonances [23]. In nanophotonic cavity

optomechanics, this modification is typically dispersive, quantified by the dispersive optomechanical coupling coefficient, $g_{\text{om}} = d\omega_o/dx$, which describes the change in the optical resonance frequency, ω_o , for a displacement, x , of the mechanical mode [3]. For mechanical modes of planar structures with vertical out-of-plane motion, such as cantilever resonances, often $g_{\text{om}} = 0$ due to the even vertical symmetry of the nanocavity optical field intensity, $|E|^2$, and the odd vertical symmetry of the mechanical-resonance-induced dielectric perturbation, $\Delta\epsilon(\mathbf{r};x)$. While fabrication imperfections or the presence of a substrate [24] can break this symmetry, the resulting g_{om} is typically small. Here we demonstrate that an optical fiber taper waveguide placed in the near field of the nanocavity can introduce both large dispersive and dissipative optomechanical coupling, whose magnitude can be tuned by adjusting the fiber position. The dispersive coupling results from the fiber distorting the vertical profile of the nanocavity field, renormalizing the optical mode of the structure. Dissipative coupling [11,16,17] is due to mechanical motion modulating the fiber–nanocavity distance, and is described by $g_e = d\gamma_e/dx$, where γ_e is the nanocavity optical mode energy decay rate into the waveguide (see Supplement 1, Section 1). This paper showcases results that build upon the demonstration of a split-beam photonic crystal nanocavity previously presented in Ref. [11] by demonstrating externally induced dispersive coupling together with larger dissipative coupling, illustrating that these parameters can be externally controlled with the fiber taper, and using this control to spatially resolve nanomechanical resonances.

The effects introduced above were studied using a split-beam photonic crystal nanocavity such as the device shown in the

scanning-electron microscopy (SEM) image in Fig. 1(a). Devices were fabricated from silicon using electron-beam lithography and reactive-ion etching to pattern the Si device layer of a silicon-on-insulator wafer, followed by selectively removing the underlying SiO₂ layer using HF wet etching. To design a split-beam cavity with a small mode volume and relatively robust performance against fabrication imperfections, we started with the grating-defect resonator design paradigm of Liu and Yariv [25], comprising end-to-end tapered Bragg gratings around a central defect that imparts a quarter-wave phase shift to the grating coupling coefficient. A split-beam cavity may then be formed by incorporating a defect with a physical gap (~ 80 nm) at cavity center; the total defect length is chosen to minimize radiative loss, as determined from finite-difference time-domain (FDTD) simulations [26]. This design supports a mode with a high optical quality factor ($Q_o \sim 10^4$) at a wavelength $\lambda_o \sim 1600$ nm, whose field profile overlaps strongly with the central gap region, as shown in Fig. 1(a). We note that an alternative design approach using elliptical holes and yielding resonant frequencies near the grating band edge is capable of much lower loss ($Q_o > 10^6$), but requires stringent control on hole dimensions [27]. Split-beam nanocavities support a variety of mechanical resonances including flexural, torsional, and rotational motion [11]. Their properties depend on how the mirrors are anchored to the surrounding chip. In the device studied here, each mirror is anchored in five locations, supporting a fundamental cantilever mode with a frequency

$f_m \sim 10$ MHz and displacement profile shown in the inset of Fig. 2(b).

The optomechanical properties of these devices were probed using a 1- μ m-diameter dimpled optical fiber taper waveguide evanescently coupled to the nanocavity near field [28]. The dimpled taper, with a nominal radius of curvature of ~ 25 μ m, was positioned using high-resolution (50 nm) motorized stepper stages, allowing it to be hovered above the nanocavity or placed in contact with either of the nanocavity mirrors [Fig. 1(b)]. The taper transmission, $T(\lambda)$, was measured using a swept-wavelength laser and a high-speed photoreceiver (Newport 1811). Optomechanical coupling was studied by measuring the spectral density of the photodetected signal, $S_{VV}(f, \lambda)$, using a real-time spectrum analyzer (Tektronix RSA5106A).

Figure 2(a) shows $T(\lambda)$ when the fiber taper is hovering ~ 500 nm above the nanocavity. The sharp dip in transmission at $\lambda_o \sim 1522$ nm results from evanescent coupling between the fiber taper and the optical mode of the nanocavity. From the linewidth, $\delta\lambda$, and minimum transmission, T_d , of this resonance, the loaded and unloaded quality factors of the device are measured to be $Q_o \sim 5200$ and $Q_i \sim 5500$, respectively. Figure 2(b) shows the power spectral density (PSD), $S_{VV}^{1/2}(f)$, of the measured fiber taper transmission signal when the input laser is red detuned at $\lambda - \lambda_o \sim \delta\lambda/2$ and the fiber taper is in contact with one of the nanocavity mirrors, labeled M1. Several sharp resonances are visible, each corresponding to optomechanical transduction of the thermal motion from mechanical resonances of the mirror not in contact with the fiber, labeled M2.

The large peak in $S_{VV}^{1/2}(f)$ at $f_m \sim 10.5$ MHz shown in Fig. 2(b) is from thermal motion and subsequent optomechanical coupling from the cantilever (C) mode of M2. When the fiber taper is positioned in a hovering configuration over the center of the cavity such that it is very close to (although not in contact

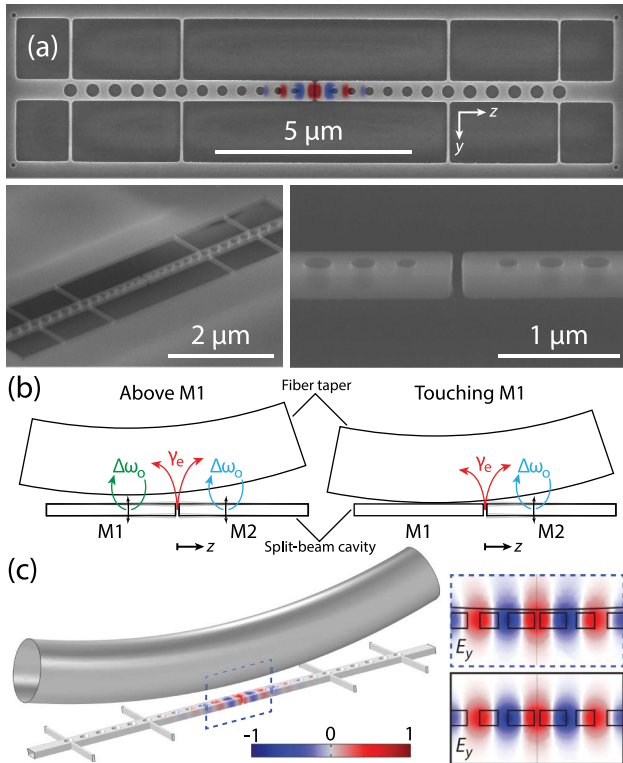


Fig. 1. (a) Scanning-electron micrographs of a split-beam photonic crystal nanocavity. The nanocavity optical mode (E_y) is superimposed on the device in the upper image. (b) Schematic of experimental geometry when fiber is hovering above (left) and touching (right) one of the mirrors. (c) Renormalization of the optical mode by the optical fiber taper. The field plots show E_y in the center of the cavity with (upper) and without (lower) the fiber taper. The red-blue scale bar indicates the normalized electric field amplitude for all figures.

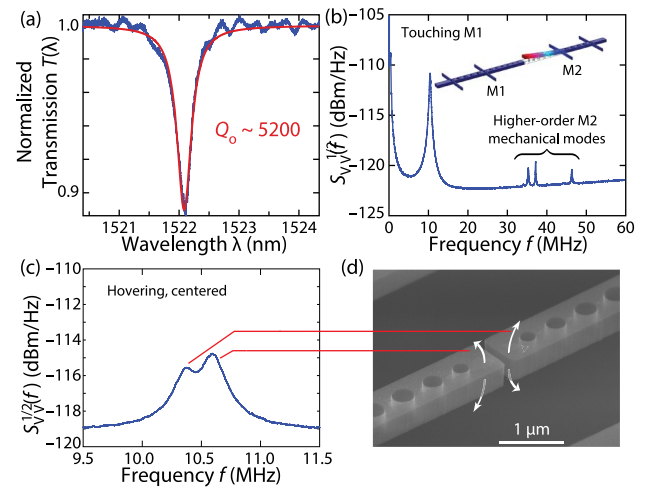


Fig. 2. (a) Fiber taper transmission under weak coupling (taper height $h \sim 500$ nm). (b) Mechanical mode spectrum when the fiber is in contact with M1. The displacement profile of the fundamental cantilever mode of M2 is shown next to the corresponding peak (amplitude greatly exaggerated). (c) Mechanical mode spectrum with the fiber hovering above the cavity center ($z_f \sim 0$), as close as possible without touching the cantilevers ($h < 150$ nm); the laser detuning was chosen to maximize the peak magnitude. Fabrication imperfections impart a ~ 200 kHz splitting between these resonances. (d) Scanning-electron micrograph of the split-beam cavity center.

with) M1 or M2, optomechanical coupling is still present, as shown in Fig. 2(c). In the hovering configuration, the peak in $S_{VV}^{1/2}(f)$ has a lower amplitude and a double-peaked structure. Each of these local maxima can be ascribed to optomechanical coupling between the nanocavity and the C mode of M1 and M2, whose mechanical frequencies, $f_1 = 10.4$ MHz and $f_2 = 10.6$ MHz, respectively, differ due to fabrication variations. In an ideal structure, small displacements of the C mode would not be transduced by the optical field, as the average refractive index sampled by the optical field varies quadratically as one of the mirrors is displaced vertically. This may be seen from the expression for g_{om} derived from perturbation theory for Maxwell's equations with shifting material boundaries [3,29]:

$$g_{om} = \frac{\omega_o}{2} \frac{\int dA \left(\frac{d\mathbf{Q}}{dx} \cdot \hat{\mathbf{n}} \right) [\Delta\epsilon |\mathbf{E}_{\parallel}|^2 - \Delta(\epsilon^{-1}) |\mathbf{D}_{\perp}|^2]}{\int dV \epsilon |\mathbf{E}|^2}, \quad (1)$$

where $\mathbf{Q}(\mathbf{r})$ is the mechanical displacement field, x is the mechanical mode amplitude, $\hat{\mathbf{n}}$ is the unit normal vector for the unperturbed cavity surface, $\Delta\epsilon = \epsilon_1 - \epsilon_2$, $\Delta(\epsilon^{-1}) = \epsilon_1^{-1} - \epsilon_2^{-1}$, and ϵ_1 and ϵ_2 are the dielectric constants of the cavity and surrounding material, respectively. For a C mode, the vertical symmetry of $\mathbf{Q}(\mathbf{r})$ is odd: motion with respect to the top and bottom surface normals of the cantilever is equal and opposite. In contrast, the optical mode energy density for the fundamental TE-like mode possesses even vertical symmetry (see Supplement 1, Section 3.A), causing g_{om} to vanish for C modes. Nonzero optomechanical coupling can be introduced by breaking the vertical symmetry of the structure. Although this can be achieved through intrinsic fabrication imperfections, the fiber taper waveguide provides an effective method for symmetry breaking via position-dependent dissipation into the waveguide and renormalization of the nanocavity field.

To gain insight into the optomechanical coupling processes responsible for the observed behavior, the nanocavity optomechanical response was measured as a function of axial fiber position z_f . When the fiber dimple is offset from the center of the nanocavity such that it is hovering above M1 ($z_f \approx -2$ μm), a single peak at f_1 is observed, as shown in Fig. 3(a). Similarly, when the fiber hovers above M2 ($z_f \approx 2$ μm), a single peak at f_2 appears. These measurements indicate that the observed optomechanical coupling is not intrinsic to the optical and mechanical modes of the nanocavity alone: the fiber position influences the optomechanical coupling processes.

The mechanism responsible for these observations can be revealed from the λ dependence of $S_{VV}^{1/2}(f, \lambda)$. Figure 3(b) shows $S_{VV}^{1/2}(f, \lambda)$ for four different fiber taper configurations: hovering above or touching M1 or M2. In all of the measurements, the maxima in $S_{VV}^{1/2}(f)$, marked by the red dotted lines, were observed at either f_1 or f_2 . In Fig. 4(a), fitting $S_{VV}^{1/2}(f_{1,2}, \lambda)$ following the procedure in [11] yields the dispersive and dissipative contributions to the total optomechanical signal.

For the hovering measurements, as λ is tuned toward the optical resonance, optomechanical coupling is observed at f_1 and f_2 when the fiber is positioned above M1 and M2, respectively, as in the fixed- λ measurements in Fig. 3(a). The maxima in $S_{VV}^{1/2}(f_{1,2}, \lambda)$ are near $\lambda \sim \lambda_o$, indicating that the optomechanical transduction mechanism is dominantly dissipative [11,30]. This is in contrast to the more commonly encountered dispersive coupling scenario observed in many nanophotonic cavity

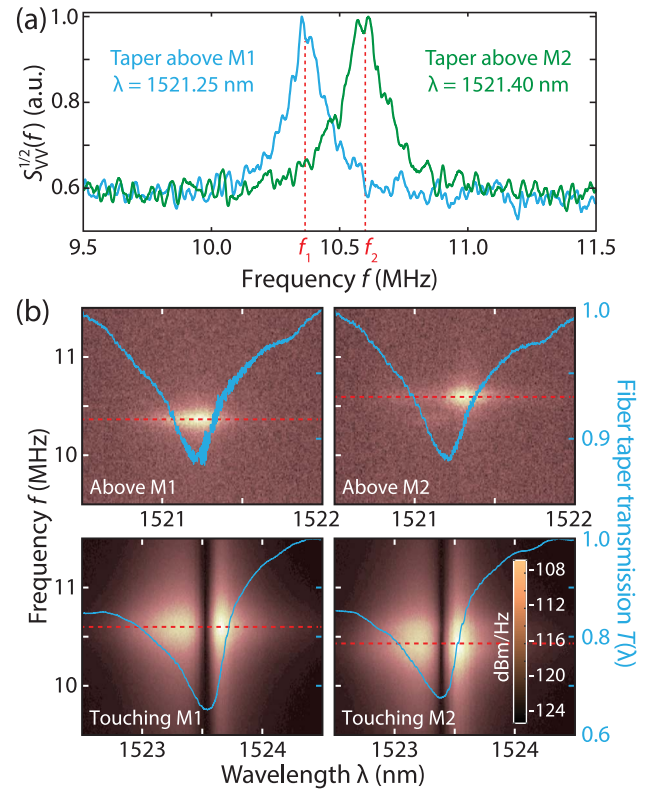


Fig. 3. (a) Mechanical spectrum $S_{VV}^{1/2}(f)$ of cantilever modes with fiber hovering ~ 250 nm above M1 (blue) and M2 (green). In each case, the wavelength was tuned to maximize the mechanical resonance. (b) $S_{VV}^{1/2}(f, \lambda)$ for the fiber hovering above/touching M1/M2, with the maxima with respect to f marked by red dotted lines. The DC fiber transmission for each configuration is shown in blue.

optomechanical systems, for which the optomechanical actuation vanishes when $\lambda = \lambda_o$. This dissipative optomechanical coupling is a result of the fiber–nanocavity coupling rate being modulated by the oscillating vertical displacement of each mirror's C mode. A full transition from dissipatively to dispersively dominated spectra is shown in Fig. 4(b), where the optomechanical signal as a function of fiber height above M2 is shown. Note that for $h < 200$ nm, fluctuations in fiber position modify λ_o , as discussed below and in Supplement 1, Section 4, blurring out the zero in the optomechanical spectrum.

When the dimpled fiber taper is in contact with mirror M1 (M2), the resonance at f_2 (f_1) is observed to dominate $S_{VV}^{1/2}(f, \lambda)$; an asymmetry in $T(\lambda)$ is also introduced due to the coupling to nonlocalized nanobeam modes, which heralds the breakdown of the ideal-coupler regime [11,31]. In this geometry, the fiber taper interacts with the optical near field and mechanical motion of the noncontacted mirror, with a separation determined by the specific shape of the fiber taper dimple, and damps the mechanical motion of the contacted mirror. In contrast to the hovering fiber taper geometry, the λ dependence of $S_{VV}^{1/2}(f, \lambda)$ in this configuration, shown in the bottom of Fig. 4(a), is observed to follow $dT(\lambda)/d\lambda$: it vanishes near resonance, indicating that dispersive coupling is the dominant optomechanical transduction mechanism. For small gaps between the fiber taper and the free nanocavity mirror, the presence of the fiber taper creates a vertically asymmetric dielectric environment [Fig. 1(c)], renormalizing the nanocavity optical mode profile

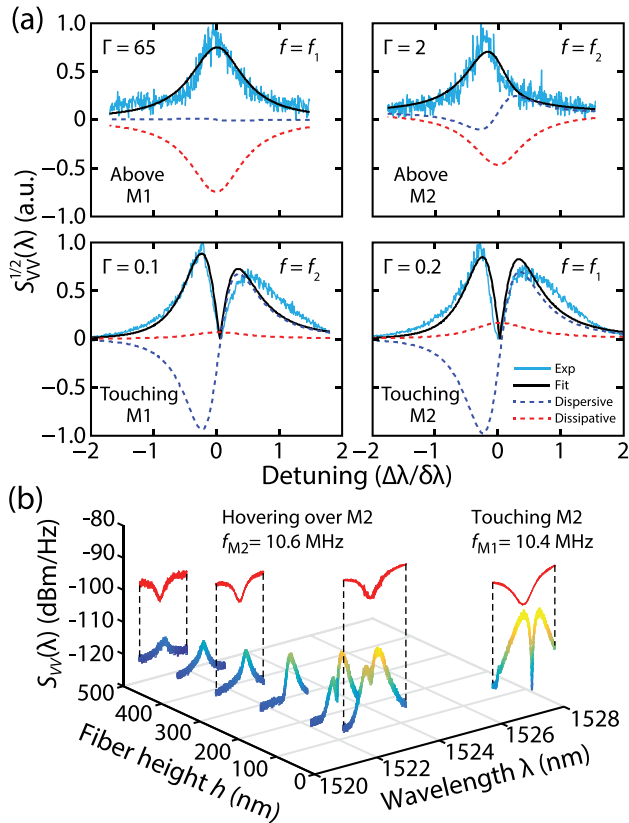


Fig. 4. (a) $S_{VV}^{1/2}$ versus detuning, $\Delta\lambda = \lambda - \lambda_0$, for the fiber hovering (upper) and touching (lower) the cantilevers, corresponding to the dotted-line slices in Fig. 3(b). The fits use the model in [11]; Γ is given by Eq. (2). (b) S_{VV} versus λ for varying h hovering over M2 ($z_f \approx 2 \mu\text{m}$) until touchdown ($h = 0$); $T(\lambda)$ is shown in red for selected heights.

and creating nonzero dispersive optomechanical coupling. Note that this renormalization manifests in a static red-shift of λ_0 by ~ 2 nm, as seen in Fig. 3(b).

The transition between predominantly dissipative and dispersive transduction can be interpreted through finite element analysis (FEA) of the optomechanical coupling as a function of vertical fiber taper position, for $z_f = 2 \mu\text{m}$ (above M2). Figure 5(a) compares the predicted and measured g_e and g_{om} as a function of taper height, h , above the nanocavity (see Supplement 1, Section 2). These simulations predict that for M2, the dispersive $g_{om}(h)$ decays exponentially with h from a maximum absolute value of ~ 3 GHz/nm, following $g_{om} \sim g_{om}^0 e^{-h/\Lambda_{om}}$ with $\Lambda_{om} \sim 75$ nm. The dissipative g_e decreases from a maximum value ~ 10 MHz/nm with decay length $\Lambda_e \sim 212$ nm. As the dispersive g_{om} decays more quickly than g_e , for small h , contributions to the optomechanical coupling from g_{om} dominate the optomechanical signal, while for large h , contributions from g_e may dominate.

The drastically different h dependence of g_{om} and g_e can be understood intuitively from perturbation theory (see Supplement 1, Section 3). In brief, the fiber perturbs the resonance frequency of the cavity ω_0 via a modification of the nanocavity's effective index. The resulting red-shift scales with the overlap of the nanocavity evanescent field intensity and the fiber dielectric [29]; g_{om} consequently shares the exponential decay length of the nanocavity evanescent field intensity. In contrast,

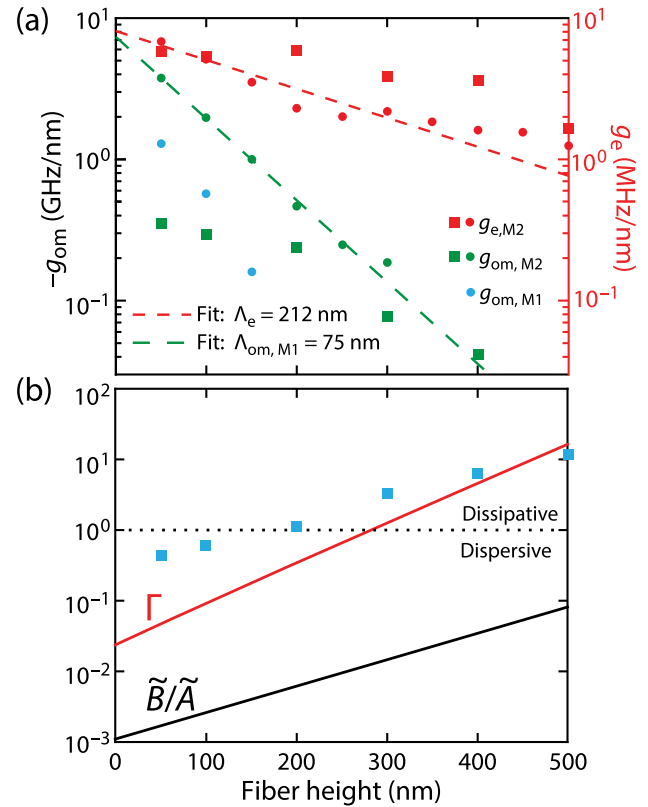


Fig. 5. (a) Simulated (circles) and experimental (squares) dispersive (g_{om}) and dissipative (g_e) coupling coefficients for the fiber dimple hovering above M2 ($z_f = 2 \mu\text{m}$). Dotted lines indicate fits to numerical simulations. Experimental values are extracted from Fig. 4(b). Simulations assume that $g_{e, M1}$ is negligible (i.e., $g_e = g_{e, M2}$) due to a relatively large separation between the fiber taper dimple and M1. (b) Simulated $\Gamma(h)$ (red line) and \tilde{B}/\tilde{A} (black line) predicted from the g_e and g_{om} values in (a). The simulated $\Gamma(h)$ also uses an approximation of the experimentally observed $T_d(h)$. Blue squares indicate experimental $\Gamma(h)$ values taken from coefficients in (a).

γ_e follows from mode coupling between the fiber and nanocavity field amplitudes [32], and therefore contains interference effects inherent to phase matching in addition to depending on the overlap of the evanescent tail of the fiber mode with the cavity. As such, the exponential decay of g_e depends critically on the effective coupling length between the dimpled fiber and the cavity, and is generally slow compared to the decay of g_{om} .

Fits to the optomechanical spectra for varying h in Fig. 4(b) provide experimental estimates of g_{om} and g_e . These values are shown in Fig. 5(a), and have good correlation with behavior from simulations for $h > 200$ nm. For small $h < 200$ nm, the accuracy of the estimates of g_{om} and g_e is reduced due to instability in λ_0 resulting from fluctuations in fiber position (see Supplement 1, Sections 1 and 4). These fluctuations reduce the visibility of the dispersive features in $S_{VV}^{1/2}(\lambda)$, and are in part driven by optical attraction or repulsion from the cavity [33]. Disagreement in observed and simulated values can also be caused by geometrical variations of the fiber. For example, if the radius of curvature of the fiber would be twice as small, simulations predict that g_{om} would be roughly halved. In addition, for small h the validity of the standard two-port fiber–nanocavity coupled mode theory (see Supplement 1, Section 1) used to predict $T(h, \lambda)$ becomes

less accurate, and parasitic effects such as insertion loss become appreciable.

The effect on the overall character of the optomechanical transduction is analyzed theoretically and experimentally in Fig. 5(b). In the sideband-unresolved regime applicable here ($\omega_m \ll \gamma_t$, where γ_t is the total nanocavity optical mode energy decay rate), the maximum dispersive and dissipative contributions to the change in optical transmission are $\frac{dT}{d\omega_o}|_{\max} = (1 - T_d)Q_o/\omega_o$ and $\frac{dT}{d\gamma_e}|_{\max} = -8T_dQ_o/\omega_o$, respectively (see Supplement 1, Section 1, and Ref. [11]). The relative balance of observed dissipative and dispersive signals may therefore be expressed by

$$\Gamma = \left| \frac{g_e \frac{dT}{d\gamma_e}|_{\max}}{g_{om} \frac{dT}{d\omega_o}|_{\max}} \right| = \frac{8g_e(h)T_d(h)}{g_{om}(h)(1 - T_d(h))}, \quad (2)$$

where $\Gamma > 1$ ($\Gamma < 1$) corresponds to a predominantly dissipative (dispersive) contribution to the $S_{VV}^{1/2}(\lambda)$ lineshape. This expression is plotted in Fig. 5(b), using the simulated values for $g_e(h)$ and $g_{om}(h)$ [Fig. 5(a)], for given T_d . Note that in the limit of weak coupling ($1 - T_d \ll 1$), $\Gamma \gg 1$ is possible even when $g_e < g_{om}$. The experimentally observed Γ for the device under study approximately follows the red line in Fig. 5(b); both theoretical and experimental Γ cross from the dispersive to the dissipative regime ($\Gamma = 1$) for $h \sim 200$ – 300 nm. This is generally consistent with the transition observed in Fig. 4(b) as well as experimental observations in Figs. 3(b) and 4(a), in which measurements show the prominence of dispersive coupling when the fiber is touching and dissipative when hovering. The respective values of Γ for the hovering configurations (upper plots in Fig. 4) indicate that h was larger for the M1 measurement than for M2: when the taper is not stabilized through contact with the device, a slow drift in h of $\sim \pm 50$ nm can occur despite the stage positions being fixed. Disagreement between simulated and measured $\Gamma(h)$ for $h < 200$ nm is ascribed to the nonidealities described above, including fluctuating taper position and λ_o , resulting in poor estimates of g_e and g_{om} .

The dramatic increase in Γ with h is promising from an optomechanical cooling standpoint, especially for systems in the sideband-unresolved regime [17–21]. Discussions of optomechanical cooling in systems exhibiting both dispersive and dissipative coupling [17,18] are typically couched in terms of the normalized coupling coefficients $\tilde{A} = \frac{-1}{\gamma_t} \frac{d\omega_o}{dx} x_{zpf}$ and $\tilde{B} = \frac{1}{\gamma_t} \frac{d\gamma_e}{dx} x_{zpf}$, where x_{zpf} is the amplitude of the zero-point fluctuations of the mechanical oscillator. The ratio $\tilde{B}/\tilde{A} = -g_e/g_{om}$ determines the optimal detuning required to minimize phonon occupation. For a given \tilde{B}/\tilde{A} and detuning, the maximum achievable optomechanical cooling rate $\gamma_{BA,opt}$, which in turn determines the minimum achievable phonon number, scales with $n\tilde{B}^2$, where n is the intracavity photon number [17], indicating that operating in a regime of large \tilde{B} is desirable in order to minimize the phonon number in a dissipatively cooled system. In contrast to Γ , $\tilde{B}/\tilde{A} < 1$ for the h range considered here [inset to Fig. 5(b)], limiting the effectiveness of dissipative cooling. However, further enhancement of the dissipative coupling strength without introducing additional parasitic loss, for example, through stronger fiber–nanocavity coupling γ_e via phase-matching considerations [34], would improve the tunability of the optomechanical coupling behavior described in this Letter

and help achieve dissipative cooling ($\gamma_{BA,opt} \propto n\tilde{B}^2$) of the C modes of this device. Given that $\tilde{B} \propto \frac{d\gamma_e}{dx} \frac{1}{\gamma_t}$, and assuming that the dissipative coupling scales as $d\gamma_e/dx \propto \gamma_e$, increasing \tilde{B} by enhancing γ_e is limited by the necessary condition that $\gamma_t \geq \gamma_e$. For the device demonstrated here, $\gamma_e/\gamma_t \sim 1/40$, indicating that increasing \tilde{B} by more than an order of magnitude through enhancement to γ_e is possible.

In summary, we have demonstrated that renormalization of the near field of a photonic crystal nanocavity can be used to induce optomechanical coupling. This enables readout of mechanical cantilever modes that otherwise have zero optomechanical coupling, and provides a spatially resolved probe of the device's mechanical modes, as well as the ability to tune the ratio of dissipative-to-dispersive coupling. Taken together, these effects have the potential to extend the range of device geometries used for optomechanics-based sensing applications, and provide opportunities for utilizing dissipative coupling to manipulate optomechanical systems.

Alberta Innovates—Technology Futures; Canada Foundation for Innovation (Fondation canadienne pour l'innovation); Natural Sciences and Engineering Research Council of Canada (Conseil de Recherches en Sciences Naturelles et en Génie du Canada).

See Supplement 1 for supporting content.

REFERENCES

1. M. Eichenfield, R. Camacho, J. Chan, K. J. Vahala, and O. Painter, "A picogram and nanometer scale photonic crystal opto-mechanical cavity," *Nature* **459**, 550–555 (2009).
2. J. Chan, M. Eichenfield, R. Camacho, and O. Painter, "Optical and mechanical design of a zipper photonic crystal optomechanical cavity," *Opt. Express* **17**, 3802–3817 (2009).
3. M. Eichenfield, J. Chan, R. Camacho, K. Vahala, and O. Painter, "Optomechanical crystals," *Nature* **462**, 78–82 (2009).
4. P. Deotare, I. Bulu, I. W. Frank, Q. Quan, Y. Zhang, R. Ilic, and M. Lončar, "All optical reconfiguration of optomechanical filters," *Nat. Commun.* **3**, 846 (2012).
5. X. Sun, J. Zhang, M. Poot, C. Wong, and H. Tang, "Femtogram doubly clamped nanomechanical resonators embedded in a high-Q two-dimensional photonic crystal nanocavity," *Nano Lett.* **12**, 2299–2305 (2012).
6. E. Gavartin, R. Braive, I. Sagnes, O. Arcizet, A. Beveratos, T. Kippenberg, and I. Robert-Philip, "Optomechanical coupling in a two-dimensional photonic crystal defect cavity," *Phys. Rev. Lett.* **106**, 203902 (2011).
7. G. Anetsberger, O. Arcizet, Q. Unterreithmeier, R. Rivière, A. Schliesser, E. Weig, J. Kotthaus, and T. Kippenberg, "Near-field cavity optomechanics with nanomechanical oscillators," *Nat. Phys.* **5**, 909–914 (2009).
8. K. Srinivasan, H. Miao, M. Rakher, M. Davaño, and V. Aksyuk, "Optomechanical transduction of an integrated silicon cantilever probe using a microdisk resonator," *Nano Lett.* **11**, 791–797 (2011).
9. A. G. Krause, M. Winger, T. D. Blasius, W. Lin, and O. Painter, "A high-resolution microchip optomechanical accelerometer," *Nat. Photonics* **6**, 768–772 (2012).
10. P. Kim, C. Doolin, B. Hauer, A. MacDonald, M. Freeman, P. Barclay, and J. Davis, "Nanoscale torsional optomechanics," *Appl. Phys. Lett.* **102**, 053102 (2013).
11. M. Wu, A. C. Hryciw, C. Healey, D. P. Lake, H. Jayakumar, M. R. Freeman, J. P. Davis, and P. E. Barclay, "Dissipative and dispersive optomechanics in a nanocavity torque sensor," *Phys. Rev. X* **4**, 021052 (2014).
12. M. Bagheri, M. Poot, M. Li, W. Pernice, and H. Tang, "Dynamic manipulation of nanomechanical resonators in the high-amplitude regime and non-volatile mechanical memory operation," *Nat. Nanotechnol.* **6**, 726–732 (2011).

13. M. Li, W. H. P. Pernice, and H. X. Tang, "Broadband all-photonic transduction of nanocantilevers," *Nat. Nanotechnol.* **4**, 377–382 (2009).
14. J. Chan, T. P. M. Alegre, A. H. Safavi-Naeini, J. T. Hill, A. Krause, S. Groblacher, M. Aspelmeyer, and O. Painter, "Laser cooling of a nanomechanical oscillator into its quantum ground state," *Nature* **478**, 89–92 (2011).
15. A. Safavi-Naeini, J. Chan, J. Hill, T. P. M. Alegre, A. Krause, and O. Painter, "Observation of quantum motion of a nanomechanical resonator," *Phys. Rev. Lett.* **108**, 033602 (2012).
16. M. Li, W. Pernice, and H. Tang, "Reactive cavity optical force on micro-disk-coupled nanomechanical beam waveguides," *Phys. Rev. Lett.* **103**, 223901 (2009).
17. F. Elste, S. Girvin, and A. Clerk, "Quantum noise interference and back-action cooling in cavity nanomechanics," *Phys. Rev. Lett.* **102**, 207209 (2009).
18. T. Weiss and A. Nunnenkamp, "Quantum limit of laser cooling in dispersively and dissipatively coupled optomechanical systems," *Phys. Rev. A* **88**, 023850 (2013).
19. Y. Liu, Y. Xiao, X. Luan, and C. Wong, "Dynamic dissipative cooling of a mechanical resonator in strong coupling optomechanics," *Phys. Rev. Lett.* **110**, 153606 (2013).
20. A. Xuereb, R. Schnabel, and K. Hammerer, "Dissipative optomechanics in a Michelson-Sagnac interferometer," *Phys. Rev. Lett.* **107**, 213604 (2011).
21. W.-J. Gu, G.-X. Li, and Y.-P. Yang, "Generation of squeezed states in a movable mirror via dissipative optomechanical coupling," *Phys. Rev. A* **88**, 013835 (2013).
22. A. Bleszynski-Jayich, W. Shanks, B. Peadercerf, E. Ginossar, F. von Oppen, L. Glazman, and J. Harris, "Persistent currents in normal metal rings," *Science* **326**, 272–275 (2009).
23. M. Aspelmeyer, T. Kippenberg, and C. Marquardt, "Cavity optomechanics," *arXiv:1303.0733* (2013).
24. M. Li, W. H. P. Pernice, C. Xiong, T. Baehr-Jones, M. Hochberg, and H. X. Tang, "Harnessing optical forces in integrated photonic circuits," *Nature* **456**, 480–484 (2008).
25. H.-C. Liu and A. Yariv, "Designing coupled-resonator optical waveguides based on high-Q tapered grating-defect resonators," *Opt. Express* **20**, 9249–9263 (2012).
26. A. F. Oskooi, D. Roundy, M. Ibanescu, P. Bermel, J. Joannopoulos, and S. G. Johnson, "Meep: a flexible free-software package for electromagnetic simulations by the FDTD method," *Comput. Phys. Commun.* **181**, 687–702 (2010).
27. A. Hryciw and P. E. Barclay, "Optical design of split-beam photonic crystal nanocavities," *Opt. Lett.* **38**, 1612–1614 (2013).
28. C. P. Michael, M. Borselli, T. J. Johnson, C. Chrystala, and O. Painter, "An optical fiber-taper probe for wafer-scale microphotonic device characterization," *Opt. Express* **15**, 4745–4752 (2007).
29. S. G. Johnson, M. Ibanescu, M. A. Skorobogatiy, O. Weisberg, J. D. Joannopoulos, and Y. Fink, "Perturbation theory for Maxwell's equations with shifting material boundaries," *Phys. Rev. E* **65**, 066611 (2002).
30. S. P. Tarabrin, H. Kaufer, F. Y. Khalili, R. Schnabel, and K. Hammerer, "Anomalous dynamic backaction in interferometers," *Phys. Rev. A* **88**, 023809 (2013).
31. I. Avrutsky, R. Gibson, J. Sears, G. Khitrova, H. M. Gibbs, and J. Hendrickson, "Linear systems approach to describing and classifying Fano resonances," *Phys. Rev. B* **87**, 125118 (2013).
32. C. Manolatou, M. J. Khan, S. Fan, P. R. Villeneuve, H. A. Haus, and J. D. Joannopoulos, "Coupling of modes analysis of resonant channel add-drop filters," *IEEE J. Quantum Electron.* **35**, 1322–1331 (1999).
33. M. Eichenfield, C. Michael, R. Perahia, and O. Painter, "Actuation of micro-optomechanical systems via cavity-enhanced optical dipole forces," *Nat. Photonics* **1**, 416–422 (2007).
34. P. E. Barclay, K. Srinivasan, M. Borselli, and O. Painter, "Efficient input and output optical fiber coupling to a photonic crystal waveguide," *Opt. Lett.* **29**, 697–699 (2004).